Heliyon 10 (2024) e23384

Contents lists available at ScienceDirect

Heliyon

journal homepage: www.cell.com/heliyon

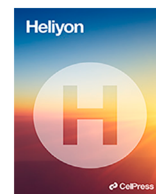

Research article

Defect engineered magnetism induction and electronic structure modulation in monolayer MoS_2

Sheikh Mohd. Ta-Seen Afrid

Department of Electrical and Electronics Engineering, Bangladesh University of Engineering and Technology, West Palashi Campus, Dhaka 1205, Bangladesh

ARTICLE INFO

Keywords:
TMD
MoS_2 vacancy
Magnetization
Band gap modulation
Optical characteristics
Defective MoS_2

ABSTRACT

The electronic, magnetic, and optical characteristics of a defective monolayer MoS_2 were examined by employing density functional theory (DFT)-based first-principles calculations. The effects of several defects on the electrical, magnetic, and optical properties, including Mo vacancies, MoS_3 vacancies, and the substitution of a single Mo atom by two S atoms were studied in this work. Our first-principles calculations revealed that different types of defects produced distinct energy states within the band gap, leading to a band gap reduction after the introduction of various types of defects, which caused a change from semiconducting to metallic behavior. The spin-up and spin-down states were separated in the case of MoS_3 vacancy. The total magnetization was $\sim -0.83\ \mu_B$/cell, and the absolute magnetization was $\sim 1.23\ \mu_B$/cell. Moreover, spin-up states had a 0.45 eV band gap, whereas spin-down states were metallic. Consequently, it can be promising for spin filter applications. It was disclosed that the broadband part of the electromagnetic spectrum has a high absorption coefficient, which is necessary for applications including impurity detection, photodiodes, and solar cells. Designing spintronic and optoelectronic devices will benefit from the modification of the electrical, optical, and magnetic properties by defect engineering of MoS_2 monolayers presented here.

1. Introduction

2D nanomaterials have become extremely popular due to their exciting electrical, optical, and magnetic properties [1–6]. Graphene, which was the very first and one of the most popular 2D materials, has band gap of 0 eV, making it a semi-metal [7]. Hence, it could not be used in switching or logical devices. Hence, the necessity of exploring other 2D materials increased. Recently, 2D-TMDs were discovered. TMDs are materials with more diverse physical characteristics than graphene. The band gap of TMD materials can be modified, providing more extra features to TMDs than graphene [8,9]. Hence, TMDs have diverse applications such as electronic, optoelectronic, spintronic, sensing, and energy-storing devices due to their promising characteristics [10–16]. Bulk TMDs are indirect band gap materials, and this property limits their application. However, TMD monolayers are direct band gap materials making them suitable for a variety of applications [17,18]. TMDs have the chemical formula MX_2. The letter M depicts an atom of a transition metal, and the letter X stands for an atom of a chalcogen. The basic unit of the layer is the X–M–X which consists of exactly 3 atomic layers. In the basic unit, the transition metal (M) layer is in the center layer, sandwiched between two chalcogen atom layers (X) [19–21]. TMDs are layered materials where the interlayers are attached by a weak force namely Van der

E-mail address: taseenafrid01@gmail.com.

https://doi.org/10.1016/j.heliyon.2023.e23384
Received 16 October 2023; Received in revised form 1 December 2023; Accepted 1 December 2023

Available online 7 December 2023
2405-8440/© 2023 The Author(s). Published by Elsevier Ltd. This is an open access article under the CC BY-NC-ND license (http://creativecommons.org/licenses/by-nc-nd/4.0/).

Waals [22–24]. Consequently, TMDs monolayers can be extracted from the bulk materials by exfoliation, which can be metallic, semi-metallic, superconducting, semiconducting, or insulating [25].

Typically TMD monolayers are non-magnetic, which limits their magnetic application. To introduce magnetism, defects can be introduced in the monolayers. Moreover, monolayer TMDs have tunable electronic properties and this fine tuning can be accomplished effectively [26–28] and adequately by defect engineering. The monolayer TMDs have a larger bandgap than the bulk TMDs. The ratio of surface area to volume in TMDs is quite high. It makes TMDs highly conducive to forming defects. The band gap of TMDs can be modulated by forming defective monolayers. Electronic, optical, and magnetic properties can be tuned by forming different kinds of defects, such as substitutional impurities and vacancies [3]. For example, defective monolayers induce magnetism and enhance the performance of electronic, optoelectronic [27,29] electrocatalytic [30–32] and photonic devices [33].

Defect engineering in TMDs involves intentionally introducing imperfections or modifying the atomic structure of these materials to enhance their properties or enable new functionalities. Several previous research works have explored numerous types of defects and their effects on the characteristics of TMDs. Point defects in TMDs include vacancies, substitutional impurities, and interstitials. Research has shown that these defects can significantly influence the electronic, optical, and magnetic properties of TMDs. Sulfur vacancies in TMD monolayers can induce localized electronic states and alter their band structure, affecting their electrical conductivity [34,35]. Substitutional doping with different elements can also tune the bandgap and electronic properties of TMDs [21,27,36–38]. Grain boundaries form when two TMD domains with different orientations meet. These interfaces can act as defect sites that affect the structural integrity and electronic properties of TMDs. Previous studies have investigated the effect of grain boundaries on charge transport, exciton dynamics, and mechanical properties of TMDs [39,40]. Understanding and controlling grain boundary formation and properties are crucial for achieving high-quality TMD films. Structural defects in TMDs can arise from missing or extra atoms, dislocations, or stacking faults. These defects have the potential to cause alterations in the structure of the crystal, affecting the material's electronic and mechanical properties [41]. For instance, dislocations can act as charge scattering centers, reducing carrier mobility in TMDs. Stacking faults can modulate the interlayer coupling and optical characteristics of TMDs. TMDs exhibit unique edge structures due to their two-dimensional nature. Defects at the edges, such as edge dislocations, can significantly impact the electronic properties and reactivity of TMDs [42]. Research has shown that edge defects can enhance catalytic activity and create localized states for various chemical reactions. Several studies have focused on passivating defects in TMDs to improve their properties [43]. Techniques such as chemical functionalization, surface treatments, and defect engineering using atomic layer deposition have been evaluated to minimize defects and boost the performance of TMD devices. Overall, previous research works on defects in TMDs have provided valuable insights into the relationship between defect structures and material properties. By understanding and manipulating defects, researchers aim to tailor the electronic, optical, and catalytic properties [44,45] of TMDs for specific applications, thereby advancing the evolution of next-generation applications and technologies.

The impacts of vacancies and substitutional impurities in the MoS_2 monolayer were investigated. The physical properties can be fine-tuned and optimized by controlling these defects for advancing different devices. Therefore, defect engineering significantly impacted the modification of the functionalities and improved the performance of the TMD materials-based devices. Defects modified band structures and other related properties were modified. *Ab initio* theoretical calculations was performed to determine the band structures, band gap, density of states (DOS), magnetization, electron localization function (ELF), and charge density difference. Moreover, Bader charge analysis was conducted and the absorption coefficient spectra was calculated. The modulation of electronic, magnetic, and optical characteristics we obtained by defect engineering has increased the probability of utilizing TMDs in diverse applications.

2. Computational details

Using the simulation tool Quantum ESPRESSO [46], which is based on density functional theory (DFT) [47], first-principles calculations were conducted to determine the electronic, optical, and magnetic properties of monolayer pristine and defective MoS_2 structures. A plane-waves basis set was used in our DFT calculations. The exchange-correlation functional Perdew-Burke-Ernzerhof (PBE) was implemented as part of the generalized gradient approximation (GGA). Ultrasoft pseudopotentials were used for molybdenum ($4s^2 4p^6 4d^4 5s^2$) and sulfur ($3s^2 3p^4$). The kinetic energy cutoff values for wave functions were established as 25 Ry, while the charge density was maintained at 225 Ry.

Monolayer MoS_2 with hexagonal symmetry (1H) was considered. A $(2 \times 2 \times 1)$ supercell of 1H-MoS_2 was created which consisted of 12 atoms. The supercell contained four molybdenum (Mo) and eight sulfur (S) atoms, as can be seen in Fig. 1. A vacuum of approximately 18 Å above the monolayer along the z direction was maintained in order to prevent interaction among periodic monolayers. Until the estimated energy error fell below the convergence threshold of 10^{-4} Ry and the forces between atoms converged to 10^{-3} Ry/Bohr, all atoms were relaxed.

In Quantum ESPRESSO, a "vacancy" typically refers to the removal of an atom from a crystal structure, creating a point defect. After the identification of the atom or species for creating a vacancy, its atomic number or species label in the crystal structure was determined. After removing an atom, the crystal structure and crystal parameters were adjusted and ensured the total charge of the system remained neutral by either adding or removing electrons accordingly. To simulate the fabricated MoS_2 monolayers with substitutional sulfur atoms and surface sulfur and molybdenum vacancies, a $(2 \times 2 \times 1)$ supercell was fully relaxed, and its lattice properties were preserved throughout all the structural relaxations that followed. The Kröger–Vink notation was used throughout the entire study [48]. Spin-polarized computations were used to examine the molecules occupying those vacancies and substitutions. Three types of fabrications were considered– (i) vacancy of a single Mo atom, V_{Mo}, (ii) vacancy of one Mo and three S atoms, V_{MoS_3}, and (iii) substitution of one W atom with two S atoms, S_{S_2}. For V_{Mo} and V_{MoS_3} calculations, a Mo atom was removed, and one

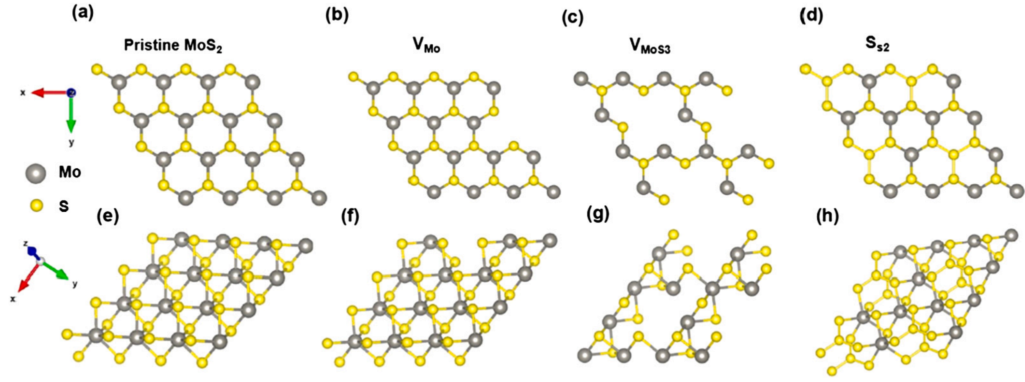

Fig. 1. XY views of monolayer (a) pristine MoS_2, (b) MoS_2 with a single Mo vacancy, (c) MoS_2 with a single Mo and three S vacancy, and (d) MoS_2 with substitution of a Mo atom with two S atoms. Perspective views of monolayer (e) pristine MoS_2, (f) MoS_2 with a single Mo vacancy, (g) MoS_2 with a single Mo and three S vacancy, and (h) MoS_2 with substitution of a Mo atom with two S atoms. Here, Mo and S atoms are colored in grey and yellow colors, respectively.

Mo atom and 3 S atoms were removed from the supercell as can be seen in Figs. 1(b) and (c), respectively. For S_{S_2} calculations, one Mo atom with 2 S atoms was replaced as shown in Fig. 1(d). After modeling, all the defective structures were optimized until convergence thresholds were achieved.

The structures were relaxed during optimization until total force and energy convergence thresholds were attained. Self-consistent field (SCF) and non-self-consistent field (NSCF) [49] calculations were conducted subsequent to relaxation in order to compute the density of states (DOS) and electronic band structures for monolayer pure and defective MoS_2. For SCF calculations (2×2×1) Monkhorst-Pack k-point grid was utilized. For occupation type, Fermi-Dirac smearing was considered, and the smearing width was 10^{-2} Ry. Spin-polarized calculations were performed to determine magnetization. During DOS and NSCF calculations, a (4×4×1) k-point grid was used. We chose the paths among the high symmetry points of the Brillouin zone of the hexagonal lattice (Γ–M–K–Γ) for calculating the band structure of pure and defective monolayers. The orbital projection of bands and estimated atomic orbital contributions were evaluated in the CBM and VBM. Moreover, it was disclosed which atomic orbitals contributed to the newly created states in the bandgap. By performing Bader charge analysis, the quantity of charge transfer between Mo and S atoms was calculated. The code developed by the Henkelman group was employed to perform Bader charge analysis [50,51]. The Bader charge transfer, $\delta\rho$, is expressed as follows:

$$\delta\rho = \rho_x - \rho_y. \tag{1}$$

In this case, ρ_x represents the electrons in the outer shell of the individual atom, and ρ_y represents the electrons in the outer shell of one of the atoms in both the pure and defective MoS_2 monolayers. Moreover, we performed the ELF and charge density difference calculations to visualize the location of charge, sharing of charge, and charge transfer.

To determine the optical properties of MoS_2 monolayers containing defects, the complex dielectric constant and absorption coefficient were evaluated. The dielectric constants' real and imaginary components were calculated using,

$$\epsilon(\omega) = \epsilon_1(\omega) + i\epsilon_2(\omega). \tag{2}$$

Here, ϵ_1 represents the real dielectric function, while ϵ_2 represents the imaginary dielectric function. The expression for the imaginary component of the frequency-dependent dielectric function denoted as ϵ_2, is as follows:

$$\epsilon_2(\omega) = \frac{4\pi^2 e^2}{\Omega} \lim_{q\to 0} \frac{1}{q^2} \sum_{c,v,k} 2\omega_k \delta(\epsilon_{ck} - \epsilon_{vk} - \omega) \times \langle u_{ck+e_\alpha q}|u_{vk}\rangle \langle u_{ck+e_\beta q}|u_{vk}\rangle^*. \tag{3}$$

In this context, α and β represent the Cartesian components, while e_α and e_β signify the unit vectors along these components. Additionally, v and c correspond to the valence and conduction band states, with ϵ_{vk} and ϵ_{ck} representing the band-edge energies of the valence and conduction bands. The cell periodic part of the orbitals at wave vector k is denoted by u_{ck}. The real part of the dielectric function, ϵ_1, is expressed as follows:

$$\epsilon_1(\omega) = 1 + \frac{2}{\pi} P \int_o^\infty \frac{\epsilon_2(\omega')\omega'}{\omega'^2 - \omega^2} d\omega'. \tag{4}$$

Here, absorption coefficient spectra, α, were derived for both pristine and defective MoS_2 monolayers by utilizing the real and imaginary components of the dielectric functions, as expressed in the equation: [52],

$$\alpha(\omega) = \frac{\sqrt{2}\omega}{c} [\sqrt{\epsilon_1{}^2(\omega) + \epsilon_2{}^2(\omega)} - \epsilon_1(\omega)]^{1/2}. \tag{5}$$

Table 1
The bond length and the bond angle of defective MoS_2 monolayers.

Structure	Mo–S Bond Length (Å)	∠S–Mo–S
Pristine	2.410	82.391°
V_{Mo}	2.431	80.189°
V_{MoS_3}	2.486	79.983°
S_{S_2}	2.413	82.438°

Here, the circular frequency is represented by ω, where $\epsilon_1(\omega)$ and $\epsilon_2(\omega)$ denote the frequency-dependent real and imaginary components of the dielectric functions, respectively. The values $\epsilon_1(\omega)$ and $\epsilon_2(\omega)$ are averages derived from the polarization vectors along the x, y, and z directions, reflecting the tensor properties of the dielectric functions.

3. Results and discussion

3.1. Effects of defects on physical structure

A (2×2×1) supercell of 1H-MoS_2 was relaxed and found that the nominal bond length of Mo-S was 2.410 Å and the nominal bond angle of the S–Mo–S bond (∠S–Mo–S) was 82.391° which agreed well with previous reports [53,54] as can be seen in Fig. 1. Due to vacancies, the bond length of the Mo-S bond increased because the number of lone pair electrons had been increased due to the creation of vacancies compared to the pristine. Lone pairs are electrons that do not participate in bonding and originate from more fully occupied antibonding orbitals. Filling antibonding orbitals reduces the bond order, leading to a decrease in bond strength and an increase in bond length. Typically, the presence of more lone pairs results in longer bonds. However, in the case of substitutional impurities, the bond length decreased as the number of lone pair electrons had decreased compared to the pristine. The ∠S-Mo-S decreased in the case of vacancies because the number of lone pair electrons had been increased for creating vacancies compared to the pure. Consequently, the repulsive forces between those lone electrons also significantly increased and for that reason, the bond angle decreased. On the other hand, in the case of substitutional impurities, ∠S-Mo-S increased because the number of lone pair electrons was lower than the pristine. Consequently, the repulsive forces between those electrons were also less than the pristine and the bond angle slightly increased. From our calculations, the bond length of Mo-S increased from 2.410 Å to 2.431 Å in the case of V_{Mo} as can be seen in Fig. 1. In the case of V_{MoS_3}, the bond length increased to 2.486 Å. However, in the case of substitutional impurities, the bond length decreased to 2.413 Å as can be seen in Fig. 1. For V_{Mo}, ∠S–Mo–S decreased from 82.391° to 80.189°. In the case of V_{MoS_3}, the ∠S–Mo–S decreased more to 79.983°. However, the bond angle increased to 82.438° for substitutional impurities as can be seen in Fig. 1. The bond angle and bond length for MoS_2 monolayers with various defects are tabulated in Table 1. The side and perspective views of pristine and defective monolayers of MoS_2 have been

3.2. Effects of defects on electronic structures

Pristine MoS_2 monolayer is a material that presents a direct band gap. However, defects were introduced such as substitutional impurities and vacancies, and the band gap of pure MoS_2 monolayer was significantly modified. Pure MoS_2 monolayer had a direct band gap of 1.82 eV, which agreed well with the previous report [55–57]. The calculated electronic structures of pure and defective MoS_2 monolayers are presented in Fig. 2. The valance band maxima and conduction band minima of pristine MoS_2 monolayer were found at K point, a high symmetry point in the Brillouin zone of a hexagonal lattice, as seen in Fig. 2(a). The most contributed atomic orbitals of valence band maxima were $d_{x^2-y^2}$ (36.8%), d_{xy} (36.8%) from Mo atoms and p_y (12%) of S atoms. The most contributed atomic orbitals of conduction band minima was d_{z^2} (80.8%) of Mo atoms as can be seen in Fig. 3(a). Atomic orbitals from S atoms made up the least contributions to VBM and CBM as can be seen in Fig. 3(e) [58].

When a single Mo atom vacancy was introduced, new energy states were created inside the band gap and some bands were found near the Fermi level. Consequently, this monolayer showed metallic behavior as shown in Fig. 2(b). The newly created states inside the band gap originated mostly from d_{z^2} (83.9%) orbitals of Mo atoms. Moreover, contributions from d_{xy}, $d_{x^2-y^2}$ orbitals of the Mo atoms were also significant. However, in the case of S atoms, p_x orbitals made up the largest contribution of 86.4% in the creation of bands around the Fermi level as can be seen in Figs. 3(b) and (f).

The MoS_3 vacancy introduced new states in the band gap; however, the number of newly created states was much higher than the defective V_{Mo} monolayer. Moreover, the band gap was zero, showing metallic behavior as shown in Fig. 2(c). Furthermore, the spin-up and spin-down bands were separated, inducing magnetism. Spin-up bands showed an indirect band gap with a bandgap of 0.45 eV whereas the spin-down bands showed metallic behavior. In the case of MoS_3 vacancy, the newly created states in the band gap originated mostly from $d_{x^2-y^2}$ (28%), d_{zx} (34.8%), d_{yz} (28%) of Mo atom. Furthermore, the contribution from d_{xy} orbital of the Mo atom was also significant. On the other hand, p_y orbitals made up the largest contribution of 42.8% for S atoms in the creation of bands around the Fermi level as can be seen in Figs. 3(c) and (g).

For the substitutional impurity, new states were also created in the band gap. As in previous cases, the zero band gap was found, which turned this structure's band structure into a metallic one, as shown in Fig. 2(d). In substituting a Mo atom with 2 S atoms, the newly created states in the band gap mostly originated from d_{xy} (81.8%) orbitals of Mo atoms. Besides, contributions from d_{zy}

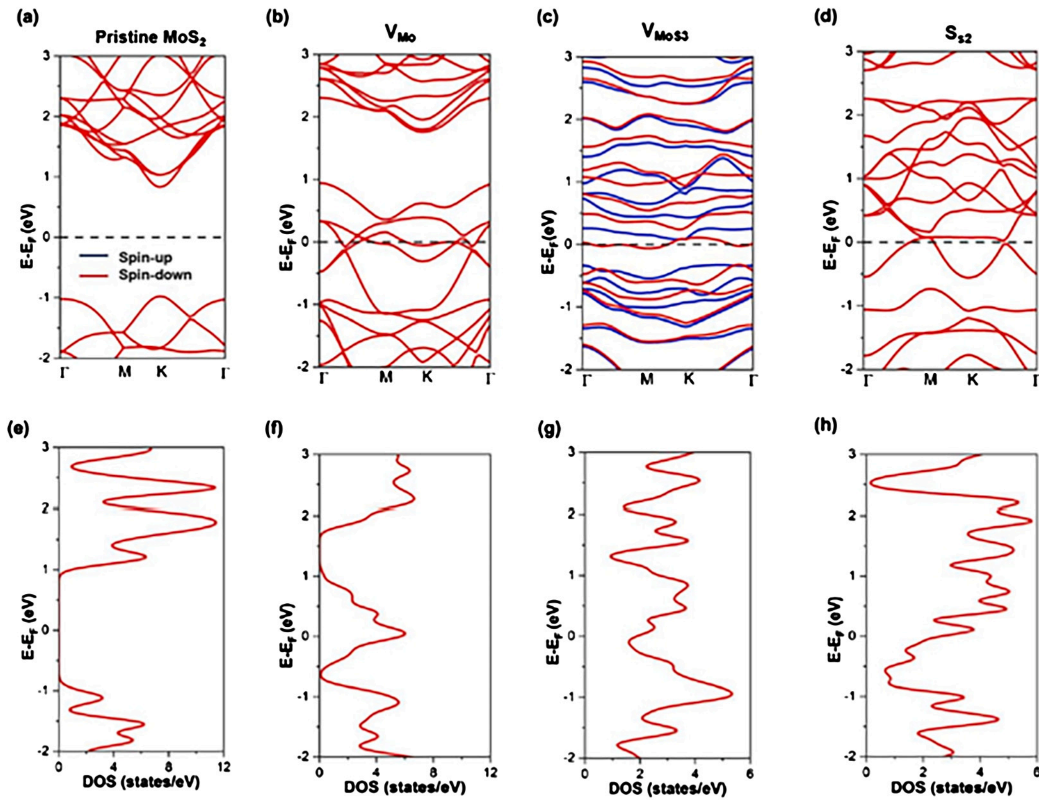

Fig. 2. Spin polarized electronic band structures of monolayer (a) pure MoS_2, (b) MoS_2 with V_{Mo} defect, (c) MoS_2 with V_{MoS_3} defect, and (d) MoS_2 with S_{S_2}. Blue indicates bands that spin up, and red indicates bands that spin down. DOS of monolayer (e) pure MoS_2, (f) MoS_2 with V_{Mo} defect, (g) MoS_2 with V_{MoS_3} defect, and (h) MoS_2 with S_{S_2}.

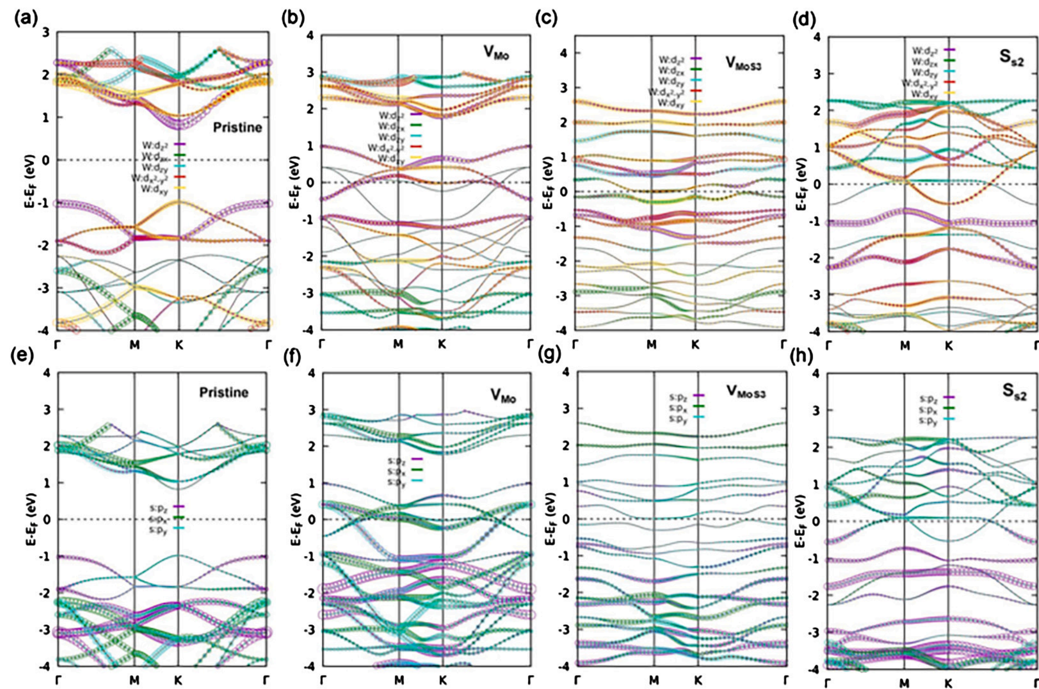

Fig. 3. Projected band structures with the contribution from d orbitals of W atoms of monolayer (a) pure MoS_2, (b) MoS_2 with V_{Mo} defect, (c) MoS_2 with V_{MoS_3} defect, and (d) MoS_2 with S_{S_2}. Projected band structures with the contribution from p orbitals of S atoms of monolayer (e) pure MoS_2, (f) MoS_2 with V_{Mo} defect, (g) MoS_2 with V_{MoS_3} defect, and (h) MoS_2 with S_{S_2}.

Table 2
Vacancy induced magnetism in MoS_2.

Structure	Total Magnetization (μ_B/cell)	Absolute Magnetization (μ_B/cell)
Pristine	0.0	0.01
V_{Mo}	0.0	0.02
V_{MoS_3}	−0.83	1.23
S_{S_2}	0.01	0.01

and d_{z^2} orbitals of the Mo atoms were also significant. However, p_z orbitals made up a remarkable contribution for S atoms in the creation of bands around the Fermi level as can be seen in Fig. 3(d) and (h).

The changes in DOS were explored due to numerous types of defects. In the case of pure MoS_2 monolayer, there was zero density of states at the Fermi-level at 0 eV. In the valence band, we found fewer peaks as well as less DOS, as shown in Fig. 2(e). However, more peaks with a more significant density of states were found in the conduction band. And the most prominent peak indicating a larger number of states was found in the conduction band. Near the Fermi level, the contribution to the DOS from Mo was higher than S, And the contribution to the DOS of S was higher than Mo in the valence band. The contribution to the DOS of Mo was higher than S in the conduction band, which matches well with previous reports [58,59].

For the V_{Mo} monolayer, the non-zero DOS at the Fermi level was found. The Fermi level shifted downward, and the Fermi level was inside the valance band. Consequently, this structure behaved as a degenerate semiconductor. More peaks in the valence band as well as a larger DOS were found due to new states as shown in Fig. 2(f). Near the Fermi level the contribution to the DOS of Mo was higher than those of S. And, the contribution to the DOS of S was higher than Mo in the vacancy-induced states. The contribution to the DOS of Mo was higher than S in the conduction band. For V_{MoS_3} monolayer, the continuous non-zero DOS was revealed through the whole energy range. The number of peaks as well as the DOS, was higher in the valence band as shown in Fig. 2(g). The largest peak indicated the largest number of states found in the valence band. A new DOS had been found at the Fermi level, and in the case of the newly created DOS, the contribution of Mo was higher than S. The contribution to the DOS of S was higher than Mo in the valence band. The contribution to the DOS of Mo was higher than S in the conduction band. In the case of S_{S_2} monolayer, the continuous non-zero DOS was found throughout the whole energy range. The largest peak indicating a large number of states was found in the valence band. The new defect-induced DOS had been found at the Fermi level as shown in Fig. 2(h) and in the case of the newly created density of states the contribution of S was higher than Mo. The contribution to the DOS of S was higher than Mo in the valence band. The contribution to the DOS of Mo was higher than S in the conduction band.

3.3. Defect induced magnetism

The magnetization of pure and defective monolayers [21,60,61] were calculated. The spin-up and spin-down states degenerated for pure MoS_2 monolayer as seen in Fig. 2(a). Hence, the total magnetization was negligible (∼ 0.0 μ_B/supercell) and the absolute magnetization was ∼ 0.01 μ_B/supercell. Similarly, there was no splitting between the spin-up and spin-down states for V_{Mo} monolayer, as shown in Fig. 2(b). Consequently, the total and absolute magnetizations were found to be insignificant.

For V_{MoS_3} monolayer, the spin-up and spin-down states were separated from each other, as can be seen in Fig. 2(c). The total magnetization was ∼ −0.83 μ_B/supercell and the absolute magnetization was ∼ 1.23 μ_B/supercell. The Mo atom of the supercell, marked in the Fig. 5(g), contributed the most to the induced magnetization. As the absolute magnetism is larger than total magnetism, it can be inferred that V_{MoS_3} monolayer was ferrimagnetic [62,63]. In the case of S_{S_2} monolayer, the total magnetization and absolute was ∼ 0.01 μ_B/supercell with degenerate spin-up and spin-down states as shown in Fig. 2(d). MoS_3 vacancy-induced magnetism, which can be utilized for diverse spintronic applications. The values of induced total magnetization and absolute magnetization for MoS_2 monolayers with numerous defects are tabulated in Table 2. Table 3 presents the amount of induced magnetism in all the atoms of V_{MoS_3} monolayer. Overall, the third Mo atom, marked as M3, had the largest amount of induced magnetism among all the Mo atoms; however, the value of magnetism was negative. On the other hand, the first S atom (S1) had the most significant amount of induced magnetism among S atoms, which was also negative.

As mentioned, spin-up and spin-down states were split, and spin-up states had a 0.45 eV band gap, whereas spin-down states were metallic for V_{MoS_3} monolayer structure. Hence, it can be promising for spin filter applications. A spin filter design based on V_{MoS_3} monolayer is demonstrated in Fig. 2(g). Randomly spin-polarized electrons tunneled from the top metal through the V_{MoS_3} monolayer spin-filter. Spin-up electrons were effectively blocked by the band gap, serving as a barrier in the spin-up channel. Conversely, spin-down electrons effortlessly tunneled through the filter, resulting in the generation of a substantial spin-polarized current within the bottom metal electrode. The barrier height for spin-up states denoted as $\Phi_\uparrow$, was approximately 0.45 eV, while for spin-down states $\Phi_\downarrow$, it was effectively 0 eV. When considering a specific barrier thickness, the spin-up tunnel current density ($J_\uparrow$) and spin-down tunnel current density ($J_\downarrow$) exhibited exponential changes with their respective barrier heights ($\Phi_{\uparrow(\downarrow)}$), following a relationship described by: [64]

$$J_{\uparrow(\downarrow)} \propto \exp(-\Phi_{\uparrow(\downarrow)}^{1/2}). \quad (6)$$

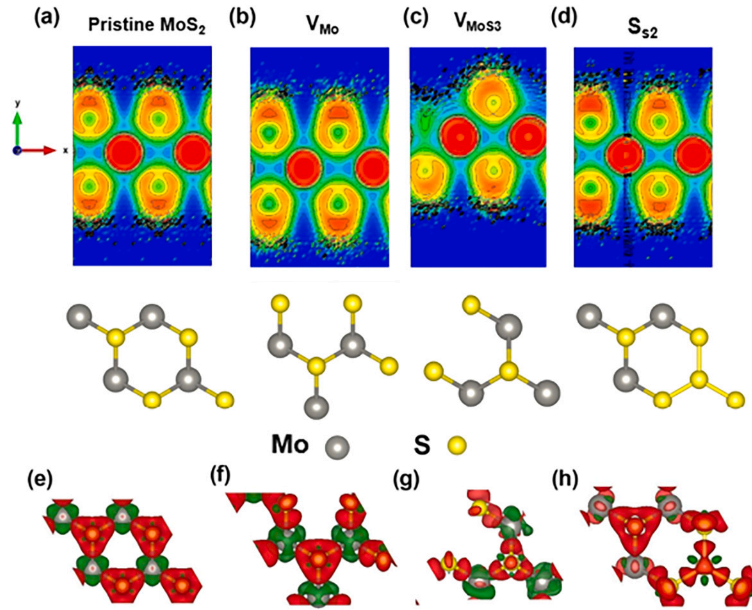

Fig. 4. ELF (electron localization function) of monolayer (a) pure MoS_2, (b) MoS_2 with V_{Mo} defect, (c) MoS_2 with V_{MoS_3} defect, and (d) MoS_2 with S_{S_2}. Charge density difference of monolayer (e) pure MoS_2, (f) MoS_2 with V_{Mo} defect, (g) MoS_2 with V_{MoS_3} defect, and (h) MoS_2 with S_{S_2}.

Table 3
Amount of induced magnetic moment for all the atoms in the supercell of V_{MoS_3} monolayer.

Atom	Amount of induced magnetism (μ_B)
M1	0.0490
M2	0.0293
M3	−0.5311
S1	−0.0202
S2	−0.0188
S3	0.0056
S4	−0.0025
S5	0.0042

Here, the exchange splitting, the difference between spin-up and spin-down electrons in terms of barrier heights was $\Phi_{\uparrow} - \Phi_{\downarrow} = 0.45$ eV. This was responsible for a very high spin-polarization, P of 32.33% in the tunnel current. P was obtained from the equation [65],

$$P = \frac{J_{\uparrow} - J_{\downarrow}}{J_{\uparrow} + J_{\downarrow}}. \quad (7)$$

In these substances, the barrier height for spin-up electrons was found to be lower than that for spin-down electrons. Nevertheless, in the scenario of a V_{MoS_3} monolayer, spin-up electrons would undergo filtration.

In Fig. 5(a)-(h), the location of the spin density among Mo and S atoms is illustrated. The red color represents spin-down density, and the blue color shows spin-up density. In the pristine case, the spin-up and spin-down densities were equally distributed around the W and S atoms, respectively. As a result, no net magnetization was found. In the case of the V_{Mo} monolayer, spin-down density around the S atoms had decreased, and a minute amount had increased the density of spin-up around the Mo atoms. Consequently, a small difference between up and down spin density was found. In the case of V_{MoS_3} monolayer, the spin-up density around Mo atoms had been significantly increased. Besides, no longer the down spin density around the S atoms was present. As a result, a significantly large difference between spin-up and spin-down densities was found. Consequently, a notable amount of magnetism was found in the V_{MoS_3} monolayer case. For S_{S_2} monolayer, a minimal difference between up and down spin density was found. As a result, a very negligible amount of magnetism was found in that case.

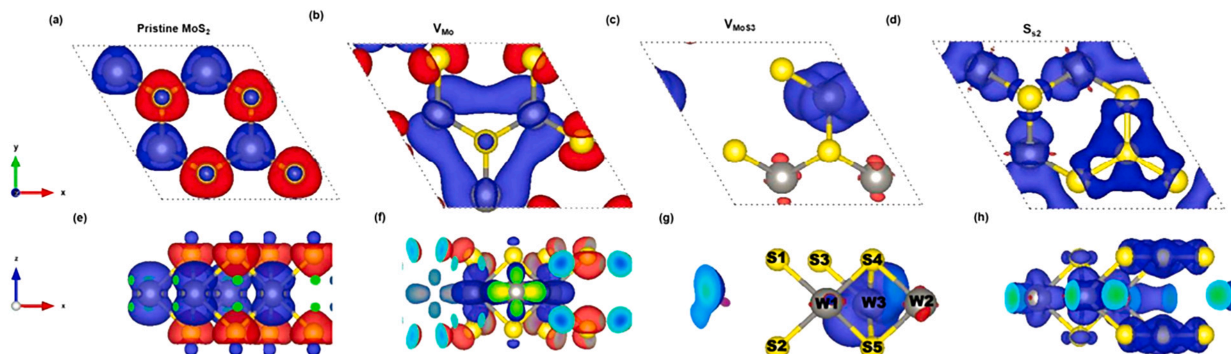

Fig. 5. XY views of spin density of monolayer (a) pure MoS_2, (b) MoS_2 with V_{Mo} defect, (c) MoS_2 with V_{MoS_3} defect, and (d) MoS_2 with S_{S_2}. ZX views of spin density of monolayer (e) pure MoS_2, (f) monolayer MoS_2 with V_{Mo} defect, (g) MoS_2 with V_{MoS_3} defect, and (h) MoS_2 with S_{S_2}.

Table 4
Change in Bader charge transfer for defective MoS_2 monolayers.

Structure	Average Bader charge of Mo (electrons/atom)	Average Bader charge of S (electrons/atom)	Average Bader charge transfer of Mo (electrons/atom)	Average Bader charge transfer of S (electrons/atom)
Pristine	12.6439	6.6780	1.3561	−0.6780
V_{Mo}	13.9701	6.0111	0.0299	−0.0111
V_{MoS_3}	12.9173	6.6496	1.0827	−0.6496
S_{S_2}	12.8382	6.3485	1.1618	−0.3485

3.4. Effect of defects on charge density

In our DFT calculations, 14 electrons for Mo and 6 for S in their valence shells were considered as mentioned in computational details. According to the Bader charge analysis, the charge was transferred to S atoms from Mo atoms. From Table 4, for the V_{Mo} monolayer, the average charge of Mo atoms was higher than all other structures. For V_{MoS_3} monolayer and S_{S_2} monolayer, the average charge of Mo was higher than pristine MoS_2. In the case of the V_{Mo} monolayer, the average charge of S atoms was lower than in all other cases. For V_{MoS_3} monolayer and S_{S_2} monolayer, the average charge of S was lower than pristine MoS_2. In the case of V_{Mo} monolayer, the net charge transfer from Mo and the net charge transfer to S was significantly lower than in any other case. In the case of V_{MoS_3} monolayer, the net charge transfer from Mo was lower than pristine MoS_2 and S_{S_2} monolayer. The net charge transfer to S was lower than pristine MoS_2 but higher than S_{S_2} monolayer in the case of V_{MoS_3} monolayer. The electron localization functions (ELFs) for different structures are shown in Figs. 4(a)-(d). In Figs. 4(a)-(d), the red color means the amount of localized electrons is high. The green color means the amount of localized electrons is medium. The blue color indicates the amount of localized electrons is null. Mo had more electrons in the valence shell than S, which was represented by a bright red circle in Figs. 4(a)-(d). However, due to vacancy, the amount of valence electrons was reduced, which can be observed in Figs. 5(b)-(d). After the creation of Mo vacancy, the reddish zone decreased. Moreover, due to vacancy, the amount of localized electrons around S atoms represented by green color also had been reduced. Typically, the green color represents a covalent bond.

In Figs. 4(e)-(h), the charge density difference of Mo and S atoms are illustrated. Here, red means accumulation of charge, and green means depletion of charge. In Figs. 4(e)-(h), the depletion of charge around the Mo atoms had been decreased as the green-colored region had been decreased for vacancies and substitutional impurities. Moreover, the depletion of charge around the S atoms had been increased as the green-colored region had been increased, which had been shown in Figs. 4(f)-(h). In the case of vacancies and substitutional impurities, the accumulation of charge around the S atoms decreased as a smaller amount decreased the red-colored region. Furthermore, the accumulation of charge around the Mo atoms had been increased as the red-colored region had been increased by a little bit amount, which had been shown in Figs. 4(f)-(h). All these findings observed from Fig. 4 were consistent with the result of the Bader charge analysis, represented in Table 4. Hence, defects significantly affected the charge density, amount of localized electrons, and charge transfer among atoms.

3.5. Effect of defects on optical properties

Defective MoS_2 monolayers showed significant modification of optical properties [66,67]. Different types of defective monolayers showed high absorption coefficients in various regions of the electromagnetic spectrum. Defects can alter the optical characteristics of a material in three primary manners. [21,68]: (i) the movement of electrons from the maxima of the valence band to vacant defect-induced states, (ii) the transition of electrons from occupied defect-induced states to the minima of the conduction band, and (iii) the shift of electrons from occupied defect-induced states to unoccupied defect-induced states. Analyzing the band structures of pure and defective MoS_2 monolayers revealed the presence of defect-induced states within the band gap. Consequently, optical

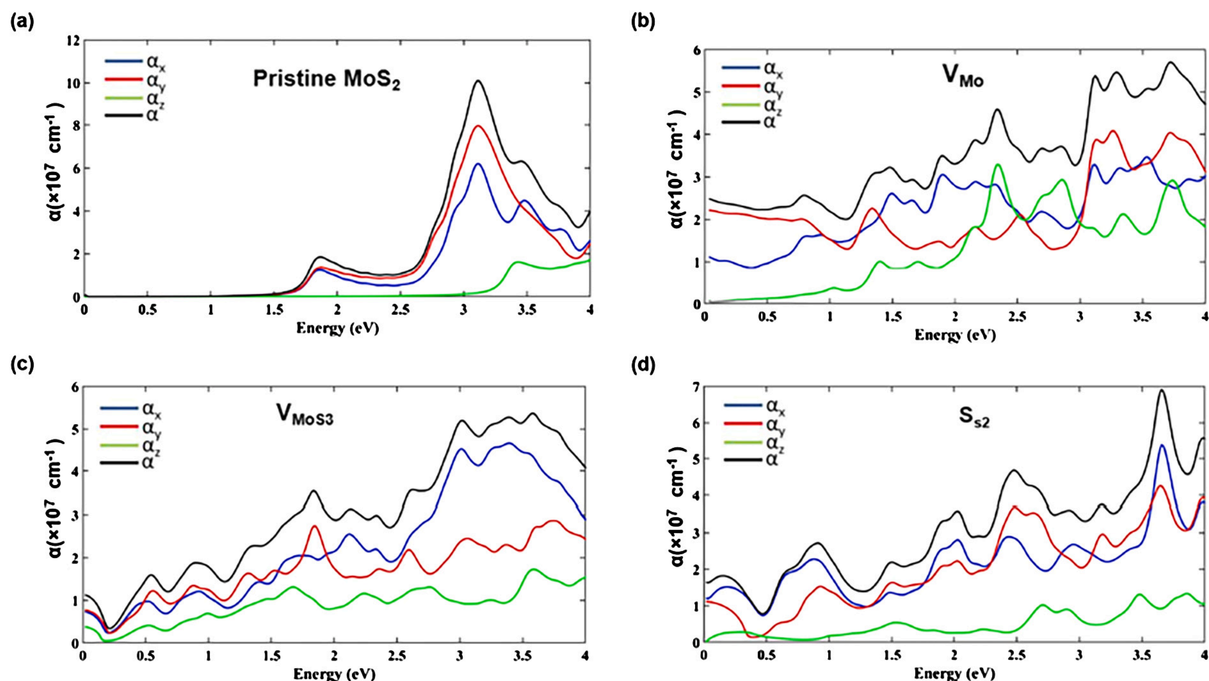

Fig. 6. Absorption coefficient of monolayer (a) pristine MoS_2, (b) MoS_2 with Mo vacancy defect, (c) MoS_2 with MoS_3 vacancy defect, and (d) MoS_2 with S_2 substitution defect.

transitions in defective MoS_2 can occur at lower photon energies owing to the existence of these defect-induced states. In Fig. 6(a) for pristine structure, the absorption coefficient was extremely high in the 3 - 3.25 eV region, which was the visible-UV region. For the V_{Mo} monolayer, a high absorption coefficient was observed [69] in the infrared to the UV regime as the Fermi level shifted inside the valance band (see Fig. 6(b)). In the case of the V_{MoS_3} monolayer, the high absorption coefficient had been observed in the region of 3 - 3.5 eV, which was also the UV region (see Fig. 6(c)). For S_{S_2} monolayer, the high absorption coefficient [70] was observed in the region of 3.5 - 3.75 eV and the UV region (see Fig. 6(d)). As a result, broadband absorption of these defective structures can be used for solar cells, photodetectors [71], photodiodes, and impurity detection applications where a high absorption coefficient is essential [66,72].

4. Conclusions

TMD monolayers are highly prone to defects due to their significant surface-to-volume ratio. Due to defects, TMD monolayers range from semiconducting to metallic behavior. In this study, *ab initio* calculations were performed to explore the electronic, magnetic, and optical properties of pristine MoS_2 and defective MoS_2 monolayers. The band gap was modulated by introducing defects. Band gap engineering will help utilize defective MoS_2 monolayers for electronic, optoelectronic, and photonic applications. Bader charge analysis was conducted to overlook the amount of charge transfer of Mo and S atoms and the absorption coefficient was evaluated. It was disclosed that defects changed charge density, bond length, bond angle, and amount of localized electrons, which will help comprehend the impact of diverse types of defects in monolayer MoS_2. Moreover, a separation between spin-up and spin-down states was found. Furthermore, spin-up states had a band gap, while spin-down states are metallic in case of MoS_3 vacancy, which will help utilize defective MoS_2 monolayers for spintronic and magnetism-related applications such as SpinFET and spin filter. High absorption coefficients in broadband regions was explored, which will be helpful for solar cell applications, photodiodes, and impurity detection applications. This work gave insights into defect engineering in MoS_2, a TMD material, which will be beneficial to propose novel electronic, optoelectronic, photonic sensing, spintronic, and energy-storage nanodevices.

Funding statement

This research did not receive any specific grant from funding agencies in the public, commercial, or not-for-profit sectors.

Additional information

No additional information is available for this paper.

CRediT authorship contribution statement

Sheikh Mohd. Ta-Seen Afrid: Writing – review & editing, Writing – original draft, Visualization, Validation, Supervision, Software, Resources, Project administration, Methodology, Investigation, Formal analysis, Conceptualization.

Declaration of competing interest

The authors declare that they have no known competing financial interests or personal relationships that could have appeared to influence the work reported in this paper.

Data availability

Data will be made available on request.

Acknowledgements

Sheikh Mohd. Ta-Seen Afrid thanks the Department of Electrical and Electronic Engineering (EEE) at Bangladesh University of Engineering and Technology (BUET) for making available the resources needed to finish their work.

References

[1] Z. Hu, Z. Wu, C. Han, J. He, Z. Ni, W. Chen, Two-dimensional transition metal dichalcogenides: interface and defect engineering, Chem. Soc. Rev. 47 (2018) 3100–3128.
[2] H. Hu, A. Zavabeti, H. Quan, W. Zhu, H. Wei, D. Chen, J.Z. Ou, Recent advances in two-dimensional transition metal dichalcogenides for biological sensing, Biosens. Bioelectron. 142 (2019) 111573.
[3] Q. Liang, Q. Zhang, X. Zhao, M. Liu, A.T. Wee, Defect engineering of two-dimensional transition-metal dichalcogenides: applications, challenges, and opportunities, ACS Nano 15 (2021) 2165–2181.
[4] M. Wu, Y. Xiao, Y. Zeng, Y. Zhou, X. Zeng, L. Zhang, W. Liao, Synthesis of two-dimensional transition metal dichalcogenides for electronics and optoelectronics, InfoMat 3 (2021) 362–396.
[5] Y. Xiao, M. Zhou, J. Liu, J. Xu, L. Fu, Phase engineering of two-dimensional transition metal dichalcogenides, Sci. China Mater. 6 (2019) 759–775.
[6] S.M.T.-S. Afrid, R. Kundu, Effect of pressure on $VTe_2/NbTe_2$ heterostructure in photonic applications: a first-principles study, in: 2023 3rd International Conference on Robotics, Electrical and Signal Processing Techniques (ICREST), IEEE, 2023, pp. 122–126.
[7] W. Oswald, Z. Wu, Energy gaps in graphene nanomeshes, Phys. Rev. B 85 (2012) 115431.
[8] A.C. Riis-Jensen, J. Lu, K.S. Thygesen, Electrically controlled dielectric band gap engineering in a two-dimensional semiconductor, Phys. Rev. B 101 (2020) 121110.
[9] M. Kang, B. Kim, S.H. Ryu, S.W. Jung, J. Kim, L. Moreschini, C. Jozwiak, E. Rotenberg, A. Bostwick, K.S. Kim, Universal mechanism of band-gap engineering in transition-metal dichalcogenides, Nano Lett. 17 (2017) 1610–1615.
[10] N.K. Nepal, L. Yu, Q. Yan, A. Ruzsinszky, First-principles study of mechanical and electronic properties of bent monolayer transition metal dichalcogenides, Phys. Rev. Mater. 3 (2019) 073601.
[11] S.M.T.-S. Afrid, N.S. Prova, First-principles calculations of pressure-tunable electronic properties of monolayer and bilayer MoX_2 (X= Te, Se), in: 2022 IEEE International Women in Engineering (WIE) Conference on Electrical and Computer Engineering (WIECON-ECE), IEEE, 2022, pp. 19–23.
[12] Q. Zeng, Z. Liu, Novel optoelectronic devices: transition-metal-dichalcogenide-based 2d heterostructures, Adv. Electron. Mater. 4 (2018) 1700335.
[13] K. Chen, J. Deng, Y. Yan, Q. Shi, T. Chang, X. Ding, J. Sun, S. Yang, J.Z. Liu, Diverse electronic and magnetic properties of CrS_2 enabling strain-controlled 2D lateral heterostructure spintronic devices, npj Comput. Mater. 7 (2021) 79.
[14] W. Cao, Q. Zhao, L. Yang, H. Cui, Enhanced NO_x adsorption and sensing properties of $MoTe_2$ monolayer by Ni-doping: a first-principles study, Surf. Interfaces 26 (2021) 101372.
[15] S.N. Upadhyay, J.A.K. Satrughna, S. Pakhira, Recent advancements of two-dimensional transition metal dichalcogenides and their applications in electrocatalysis and energy storage, Emerg. Mater. 4 (2021) 951–970.
[16] A. Raza, U. Qumar, A. Haider, S. Naz, J. Haider, A. Ul-Hamid, M. Ikram, S. Ali, S. Goumri-Said, M.B. Kanoun, Liquid-phase exfoliated MoS_2 nanosheets doped with p-type transition metals: a comparative analysis of photocatalytic and antimicrobial potential combined with density functional theory, Dalton Trans. 50 (2021) 6598–6619.
[17] C. Lin, L. Cai, J.-H. Fu, S. Sattar, Q. Wang, Y. Wan, C.-C. Tseng, C.-W. Yang, A. Aljarb, K. Jiang, et al., Direct band gap in multilayer transition metal dichalcogenide nanoscrolls with enhanced photoluminescence, ACS Mater. Lett. 4 (2022) 1547–1555.
[18] Y. Guo, B. Li, Y. Huang, S. Du, C. Sun, H. Luo, B. Liu, X. Zhou, J. Yang, J. Li, et al., Direct bandgap engineering with local biaxial strain in few-layer MoS_2 bubbles, Nano Res. 13 (2020) 2072–2078.
[19] X. Chia, M. Pumera, Layered transition metal dichalcogenide electrochemistry: journey across the periodic table, Chem. Soc. Rev. 47 (2018) 5602–5613.
[20] S.M.T.-S. Afrid, et al., Impact of vacancies in monolayer 1T-$TiTe_2$ for optoelectronic and spintronic applications: a first-principles study, in: 2023 International Conference on Electrical, Computer and Communication Engineering (ECCE), IEEE, 2023, pp. 1–5.
[21] S.M.T.-S. Afrid, N.S. Prova, A DFT study on vacancy induced VSe_2 monolayer for optoelectronic and spintronic devices, in: 2022 IEEE International Women in Engineering (WIE) Conference on Electrical and Computer Engineering (WIECON-ECE), IEEE, 2022, pp. 212–216.
[22] Y. Jiang, S. Chen, W. Zheng, B. Zheng, A. Pan, Interlayer exciton formation, relaxation, and transport in TMD van der Waals heterostructures, Light: Sci. Appl. 10 (2021) 72.
[23] H. Qi, L. Wang, J. Sun, Y. Long, P. Hu, F. Liu, X. He, Production methods of van der Waals heterostructures based on transition metal dichalcogenides, Crystals 8 (2018) 35.
[24] S.M.T.-S. Afrid, Effect of external electric field on stability and electrical properties of monolayer WSTe alloy, in: 2022 4th International Conference on Electrical, Computer & Telecommunication Engineering (ICECTE), IEEE, 2022, pp. 115–118.
[25] H. Huang, X. Fan, D.J. Singh, W. Zheng, Recent progress of TMD nanomaterials: phase transitions and applications, Nanoscale 12 (2020) 1247–1268.
[26] M. Fang, E.-H. Yang, Advances in two-dimensional magnetic semiconductors via substitutional doping of transition metal dichalcogenides, Materials 16 (2023) 3701.

[27] N. Guo, X. Fan, Z. Chen, Z. Luo, Y. Hu, Y. An, D. Yang, S. Ma, Electronic and magnetic properties of group-V TMDs monolayers with defects: a first-principles study, Comput. Mater. Sci. 176 (2020) 109540.
[28] F. Yang, P. Hu, F.F. Yang, B. Chen, F. Yin, R. Sun, K. Hao, F. Zhu, K. Wang, Z. Yin, Emerging enhancement and regulation strategies for ferromagnetic 2D transition metal dichalcogenides, Adv. Sci. 10 (2023) 2300952.
[29] J. Hong, C. Jin, J. Yuan, Z. Zhang, Atomic defects in two-dimensional materials: from single-atom spectroscopy to functionalities in opto-/electronics, nanomagnetism, and catalysis, Adv. Mater. 29 (2017) 1606434.
[30] J. Li, T. Joseph, M. Ghorbani-Asl, S. Kolekar, A.V. Krasheninnikov, M. Batzill, Edge and point-defect induced electronic and magnetic properties in monolayer $PtSe_2$, Adv. Funct. Mater. 32 (2022) 2110428.
[31] A. Habib, M. Ikram, A. Haider, A. Ul-Hamid, I. Shahzadi, J. Haider, M.B. Kanoun, S. Goumri-Said, W. Nabgan, Experimental and theoretical study of catalytic dye degradation and bactericidal potential of multiple phase Bi and MoS_2 doped SnO_2 quantum dots, RSC Adv. 13 (2023) 10861–10872.
[32] A. Raza, J. Hassan, M. Ikram, S. Naz, A. Haider, A. Ul-Hamid, I. Shahzadi, J. Haider, S. Goumri-Said, M. Kanoun, et al., Molecular docking and dft analyses of magnetic cobalt doped MoS_2 and BN nanocomposites for catalytic and antimicrobial explorations, Surf. Interfaces 27 (2021) 101571.
[33] R. Chua, J. Yang, X. He, X. Yu, W. Yu, F. Bussolotti, P.K.J. Wong, K.P. Loh, M.B. Breese, K.E.J. Goh, et al., Can reconstructed Se-deficient line defects in monolayer VSe_2 induce magnetism?, Adv. Mater. 32 (2020) 2000693.
[34] D. Edelberg, D. Rhodes, A. Kerelsky, B. Kim, J. Wang, A. Zangiabadi, C. Kim, A. Abhinandan, J. Ardelean, M. Scully, et al., Approaching the intrinsic limit in transition metal diselenides via point defect control, Nano Lett. 19 (2019) 4371–4379.
[35] Y.J. Zheng, Y. Chen, Y.L. Huang, P.K. Gogoi, M.-Y. Li, L.-J. Li, P.E. Trevisanutto, Q. Wang, S.J. Pennycook, A.T. Wee, et al., Point defects and localized excitons in 2D WSe_2, ACS Nano 13 (2019) 6050–6059.
[36] K. Zhang, J. Robinson, Doping of two-dimensional semiconductors: a rapid review and outlook, MRS Adv. 4 (2019) 2743–2757.
[37] W.H. Lee, Y.D. Park, Tuning electrical properties of 2D materials by self-assembled monolayers, Adv. Mater. Interfaces 5 (2018) 1700316.
[38] M. Ikram, B. Ilyas, A. Haider, J. Haider, A. Ul-Hamid, A. Shahzadi, S. Goumri-Said, M.B. Kanoun, W. Nabgan, A. Mahmood, Fabrication of La-doped MoS_2 nanosheets with tuned bandgap for dye degradation and antimicrobial activities, experimental and computational investigations, Adv. Mater. Interfaces (2023) 2202404.
[39] W. Zhou, X. Zou, S. Najmaei, Z. Liu, Y. Shi, J. Kong, J. Lou, P.M. Ajayan, B.I. Yakobson, J.-C. Idrobo, Intrinsic structural defects in monolayer molybdenum disulfide, Nano Lett. 13 (2013) 2615–2622.
[40] S. Cai, W. Zhao, A. Zafar, Z. Wu, Y. Tao, K. Bi, Z. Wei, Z. Ni, Y. Chen, Photoluminescence characterization of the grain boundary thermal stability in chemical vapor deposition grown WS_2, Mater. Res. Express 4 (2017) 106202.
[41] J.G. DiStefano, A.A. Murthy, H.J. Jung, R. dos Reis, V.P. Dravid, Structural defects in transition metal dichalcogenide core-shell architectures, Appl. Phys. Lett. 118 (2021).
[42] Y. Zhao, X. Kong, M.J. Shearer, F. Ding, S. Jin, Chemical etching of screw dislocated transition metal dichalcogenides, Nano Lett. 21 (2021) 7815–7822.
[43] J.H. Park, A. Sanne, Y. Guo, M. Amani, K. Zhang, H.C. Movva, J.A. Robinson, A. Javey, J. Robertson, S.K. Banerjee, et al., Defect passivation of transition metal dichalcogenides via a charge transfer van der Waals interface, Sci. Adv. 3 (2017) e1701661.
[44] Z. Hai, J. Du, M.K. Akbari, C. Xue, H. Xu, S. Zhuiykov, Carbon-doped MoS_2 nanosheet photocatalysts for efficient degradation of methyl orange, Ionics 23 (2017) 1921–1925.
[45] X. Ma, J. Hu, M. Zheng, D. Li, H. Lv, H. He, C. Huang, N_2 reduction using single transition-metal atom supported on defective WS_2 monolayer as promising catalysts: a DFT study, Appl. Surf. Sci. 489 (2019) 684–692.
[46] P. Giannozzi, O. Andreussi, T. Brumme, O. Bunau, M.B. Nardelli, M. Calandra, R. Car, C. Cavazzoni, D. Ceresoli, M. Cococcioni, et al., Advanced capabilities for materials modelling with Quantum ESPRESSO, J. Phys. Condens. Matter 29 (2017) 465901.
[47] A. Yoshimura, M. Lamparski, N. Kharche, V. Meunier, First-principles simulation of local response in transition metal dichalcogenides under electron irradiation, Nanoscale 10 (2018) 2388–2397.
[48] C. Koyama, J. Nozawa, K. Fujiwara, S. Uda, Effect of point defects on Curie temperature of lithium niobate, J. Am. Ceram. Soc. 100 (2017) 1118–1124.
[49] X.-M. Zhang, J. Tang, J. Zhang, J. Yu, L. Sun, Z. Yang, K. Xia, W. Sun, A novel two-dimensional superconducting Ti layer: density functional theory and electron-beam irradiation, Nanoscale Horiz. 8 (2023) 767–775.
[50] W. Tang, E. Sanville, G. Henkelman, A grid-based Bader analysis algorithm without lattice bias, J. Phys. Condens. Matter 21 (2009) 084204.
[51] C.-S. Lin, A.-Y. Zhou, W.-D. Cheng, N. Ye, G.-L. Chai, Atom-resolved analysis of birefringence of nonlinear optical crystals by Bader charge integration, J. Phys. Chem. C 123 (2019) 31183–31189.
[52] S.M. Ramay, S.M. Ali, H. Kassim, M.S. Amer, Ab-initio and experimental studies for the electronic and optical response of Zn–MoS_2 thin films, Physica B, Condens. Matter 628 (2022) 413558.
[53] L. Wei, C. Jun-fang, H. Qinyu, W. Teng, Electronic and elastic properties of MoS_2, Physica B, Condens. Matter 405 (2010) 2498–2502.
[54] D. Liu, X. Chen, D. Li, F. Wang, X. Luo, B. Yang, Simulation of MoS_2 crystal structure and the experimental study of thermal decomposition, J. Mol. Struct. 980 (2010) 66–71.
[55] S. Das, Y. Wang, Y. Dai, S. Li, Z. Sun, Ultrafast transient sub-bandgap absorption of monolayer MoS_2, Light: Sci. Appl. 10 (2021) 27.
[56] D. Lloyd, X. Liu, J.W. Christopher, L. Cantley, A. Wadehra, B.L. Kim, B.B. Goldberg, A.K. Swan, J.S. Bunch, Band gap engineering with ultralarge biaxial strains in suspended monolayer MoS_2, Nano Lett. 16 (2016) 5836–5841.
[57] J. Ryou, Y.-S. Kim, S. Kc, K. Cho, Monolayer MoS_2 bandgap modulation by dielectric environments and tunable bandgap transistors, Sci. Rep. 6 (2016) 29184.
[58] L. Xian, M. Claassen, D. Kiese, M.M. Scherer, S. Trebst, D.M. Kennes, A. Rubio, Realization of nearly dispersionless bands with strong orbital anisotropy from destructive interference in twisted bilayer MoS_2, Nat. Commun. 12 (2021) 5644.
[59] Y. Xie, X. Li, Y. Wang, B. Li, L. Yang, N. Zhao, M. Liu, X. Wang, Y. Yu, J.-M. Liu, Reaction mechanisms for reduction of CO_2 to CO on monolayer MoS_2, Appl. Surf. Sci. 499 (2020) 143964.
[60] R. Sanikop, C. Sudakar, Tailoring magnetically active defect sites in MoS_2 nanosheets for spintronics applications, ACS Appl. Nano Mater. 3 (2019) 576–587.
[61] H. Ren, G. Xiang, Strain-modulated magnetism in MoS_2, Nanomaterials 12 (2022) 1929.
[62] Y. Chen, S. Huang, X. Ji, K. Adepalli, K. Yin, X. Ling, X. Wang, J. Xue, M. Dresselhaus, J. Kong, et al., Tuning electronic structure of single layer MoS_2 through defect and interface engineering, ACS Nano 12 (2018) 2569–2579.
[63] M. Zhang, Q. Li, W. Cheng, Y. Gao, B. Liao, M. Ying, Robust room-temperature ferromagnetism induced by defect engineering in monolayer MoS_2, Appl. Surf. Sci. 608 (2023) 155220.
[64] S.-C. Chang, S. Manipatruni, D.E. Nikonov, I.A. Young, A. Naeemi, Design and analysis of Si interconnects for all-spin logic, IEEE Trans. Magn. 50 (2014) 1–13.
[65] M.R. Osanloo, A. Saadat, M.L. Van de Put, A. Laturia, W.G. Vandenberghe, Transition-metal nitride halide dielectrics for transition-metal dichalcogenide transistors, Nanoscale 14 (2022) 157–165.
[66] D.K. Singh, R. Pant, A.M. Chowdhury, B. Roul, K.K. Nanda, S.B. Krupanidhi, Defect-mediated transport in self-powered, broadband, and ultrafast photoresponse of a MoS_2/AlN/Si-based photodetector, ACS Appl. Electron. Mater. 2 (2020) 944–953.
[67] M. Zumuukhorol, Z. Khurelbaatar, D.-H. Kim, K.-H. Shim, V. Janardhanam, V.R. Reddy, C.-J. Choi, Broadband photodetector based on MoS_2/Ge heterojunction for optoelectronic applications, Vacuum 209 (2023) 111746.
[68] T. Amit, D. Hernangómez-Pérez, G. Cohen, D.Y. Qiu, S. Refaely-Abramson, Tunable magneto-optical properties in MoS_2 via defect-induced exciton transitions, Phys. Rev. B 106 (2022) L161407.

[69] P.M. MC de Melo, Z. Zanolli, M.J. Verstraete, Optical signatures of defect centers in transition metal dichalcogenide monolayers, Adv. Quantum Technol. 4 (2021) 2000118.

[70] Y. Zhu, J. Lim, Z. Zhang, Y. Wang, S. Sarkar, H. Ramsden, Y. Li, H. Yan, D. Phuyal, N. Gauriot, et al., Room-temperature photoluminescence mediated by sulfur vacancies in 2D molybdenum disulfide, ACS Nano 17 (2023) 13545–13553.

[71] Y. Lu, T. Chen, N. Mkhize, R.-J. Chang, Y. Sheng, P. Holdway, H. Bhaskaran, J.H. Warner, GaS: WS_2 heterojunctions for ultrathin two-dimensional photodetectors with large linear dynamic range across broad wavelengths, ACS Nano 15 (2021) 19570–19580.

[72] V. Kaushik, D. Varandani, P. Das, B. Mehta, Layer dependent photoresponse behavior of chemical vapor deposition synthesized MoS_2 films for broadband optical sensing, J. Phys. D, Appl. Phys. 52 (2019) 475302.